Geophysical Journal International

Geophys. J. Int. (2016) **206,** 1645–1651
Advance Access publication 2016 June 29
GJI Seismology

doi: 10.1093/gji/ggw236

Structure of the Los Angeles Basin from ambient noise and receiver functions

Yiran Ma and Robert W. Clayton

Seismological Laboratory, California Institute of Technology, Pasadena, CA 91125*, USA. E-mail: yrma@caltech.edu*

Accepted 2016 June 20. Received 2016 June 18; in original form 2016 March 29

SUMMARY

A velocity (*Vs*) and structure model is derived for the Los Angeles Basin, California based on ambient-noise surface wave and receiver-function analysis, using data from a low-cost, short-duration, dense broad-band survey (LASSIE) deployed across the basin. The shear wave velocities show lateral variations at the Compton-Los Alamitos and the Whittier Faults. The basement beneath the Puente Hills–San Gabriel Valley shows an unusually high velocity ($\sim$4.0 km s^{-1}) and indicates the presence of schist. The structure of the model shows that the basin is a maximum of 8 km deep along the profile and that the Moho rises to a depth of 17 km under the basin. The basin has a stretch factor of 2.6 in the centre grading to 1.3 at the edges and is in approximate isostatic equilibrium.

Key words: Interferometry; Interface waves; Seismic tomography.

1 INTRODUCTION

The Los Angeles Basin is a Miocene-age pull-apart basin that was formed by the passing of the Pacific-Juan de Fuca-North America triple junction by southern California (Nicholson *et al.* 1994; Ingersoll & Rumelhart 1999). Ingersoll & Rumelhart (1999) have proposed a three-stage model for its evolution, including transrotation (18–12 Ma), transtension (12–6 Ma) and transpression (6–0 Ma) episodes. The LA Basin has been extensively studied over the last few decades because it is a significant oil-production area (Wright 1991), and because it is a major concern for the seismic hazard evaluation for the area (Olsen 2000; Komatitsch *et al.* 2004). The basin is part of the seismic hazard because the sediments trap and amplify strong motion energy, and because of its size and depth, the basin is capable of enhancing waves in the 2–5 s range, which is particularly dangerous for the high-rise buildings in the area. Numerical modeling of these phenomena requires an accurate model of the subsurface structure and velocities that define the Los Angeles Basin.

An initial unified model for the southern California region was produced by Magistrale *et al.* (2000) with a mixture of various studies such as receiver functions (RFs; Zhu & Kanamori 2000) and tomography (Hauksson 2000). The basin structure was based on empirical rules applied to formation maps that were interpolated from borehole data. Another approach was used in Süss & Shaw (2003), where they used *P*-wave velocity measurements determined from stacking velocities from oil-company reflection surveys and sonic logs from boreholes, along with a basin shape model based on gravity and borehole lithology observations (McCulloh 1960; Yerkes *et al.* 1965). These models have been combined and further enhanced through the use of full waveform inversions (Tape *et al.* 2009; Lee *et al.* 2014), leading to an updated unified model (Shaw *et al.* 2015) including the CVM-H velocity model (currently 15.1.0 version) and the CFM fault model. Fig. S1 in the Supporting Information shows the CVM-H model beneath the array. The shallow structure (less than 10 km depth) shows significant lateral variation, while the deeper part is almost constant except for a slight dip on the Moho.

In this paper, we add some additional constraints on the structure of the Los Angeles Basin and its shear wave velocities. This study is based on a new survey that was done in the fall of 2014. It consisted of a relatively dense array of broad-band sensors that traversed the basin from Long Beach, through Whittier to the southern part of the San Gabriel Valley. Fig. 1 shows the location of the experiment, which is named 'Los Angeles Syncline Seismic Interferometry Experiment' (LASSIE). It includes 73 three-component broad-band stations, 51 of which are deployed in a line with $\sim$1 km interstation distance. They were operational from 2014 September to November, with average recording time of about 40 d. This survey is an example of what can be done with a low-cost, short-duration, rapid-deployment style that may prove useful for conducting additional surveys to refine the basin model.

We use ambient-noise-derived surface waves and RFs to construct the new model. Both are traditionally thought of as not being very useful in an urban environment where the cultural noise can be overwhelming, and the basin reverberations can make it difficult to identify the various phases in the RFs. However, as shown here, an excellent signal can be obtained and the key is to have a dense array to use lateral continuity to distinguish the interface signals from the noise.

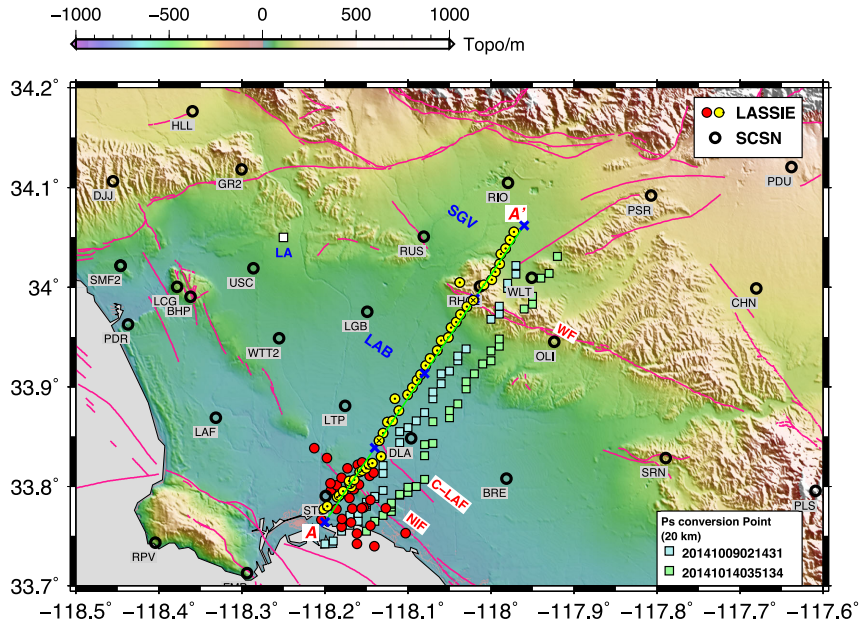

Figure 1. The LASSIE array. The yellow and red dots are LASSIE stations, and the black circles are SCSN stations. The green line denotes the location of the 2-D profile (A–A′), and the distances from A are marked with blue crosses in 10 km intervals. The faults are shown in pink lines (Jennings & Bryant 2010). LA: Los Angeles, LAB: Los Angeles Basin, SGV: San Gabriel Valley, NIF: Newport-Inglewood Fault, C-LAF: Compton-Los Alamitos Fault, WF: Whittier Fault. The *Ps* conversion points at 20 km depth are plotted for the two events used in the receiver functions (Fig. 2).

Table 1. Events with clear recordings. The top two events happened during most stations were in operation, and are used in the receiver-function analysis.

Time*	Latitude (°)	Longitude (°)	Depth (km)	Magnitude	Backazimuth (°)	Distance (°)
20141009021431	–32.1082	–110.811	16.54	7	173.231	66.0076
20141014035134	12.5262	–88.1225	40	7.3	120.746	34.5917
20140924111615	–23.8009	–66.6321	224	6.2	132.236	75.4109
20141101185722	–19.6903	–177.759	434	7.1	236.282	77.8924

*Time is in the format of YYYYMMDDHHMMSS.

2 RECEIVER FUNCTIONS

Standard methods are used to retrieve and process the RFs (Ma & Clayton 2015). For each seismic event, the data are rotated to R-T-Z coordinates and filtered to a 1–50 s passband. An iterative time-domain deconvolution (Ligorría & Ammon 1999) is used to retrieve the *P*-to-*S* RFs. A low-pass Gaussian filter is applied with a parameter of 2.5, which means the corresponding cut-off frequency is ∼1.2 Hz and the pulse width in time domain is ∼1.0 s (see the Supporting Information). The events we used are within a 30°–95° epicentral distance, and have magnitude no less than 6. Two events (Table 1) with clear recordings occurred while most stations were in operation, and are used in the following processing. Their approximate *Ps* conversion points at 20 km depth are shown in Fig. 1.

The time-domain RFs are shown in Fig. 2. The *PpPs* multiples corresponding to the basement depth, are recognized after converting the time axis to depth using the time–depth relation for the *PpPs* phase (Fig. S2, Supporting Information). The common conversion point (CCP) migration (Zhu 2000) result using the *PpPs* phase is shown in Fig. 3. For each station, we use the 1-D model extracted from CVM-H model at the station location as the reference model for time–depth conversion, which takes account of the anomalously high *Vp*/*Vs* ratio for the sedimentary layer (see fig. 3 in Brocher 2005). An underestimation of the *Vp*/*Vs* ratio can result in a deeper depth of the structure (Zhu & Kanamori 2000). In the absence of a good reference model, we could first do the CCP migration with a model without a sedimentary layer (e.g. IASP91 model), then use the RF results to update the reference model using an empirical *Vp*/*Vs* ratio for the sedimentary layer. To estimate the horizontal resolution of the CCP image, we consider the first Fresnel zone as $\frac{1}{4}$ of the wavelength, which is $\sqrt{1/2\lambda z}$. For a wavelength of 3.5 km (corresponding to 1-s *S* wave with velocity of 3.5 km s^{-1}), it is about 4 km at $z = 10$ km and is about 6 km at $z = 20$ km. Accordingly, in Fig. 3, we use a bin width of 1.5 km for depth less than 12 km to image the basement and 3.0 km for deeper depth to image the Moho.

We observe a clear basement shape that is generally in accordance with the CVM-H model (Fig. S1, Supporting Information). In addition, we observe strong thinning of the crust beneath the basin, which is very different from the CVM-H model, but is more consistent with the large-magnitude crustal extension that formed the basin (Crouch & Suppe 1993; Ingersoll & Rumelhart 1999).

For comparison, we also show the RFs calculated for the DLA station of the SCSN, which is located in the basin and is close to the A–A′ profile (Fig. 1). With two years of data, we have ∼100 events for the RFs (Fig. S3, Supporting Information). We see that despite the large number of events and good azimuthal coverage, the useful phases (e.g. the Moho *Ps*) are very difficult to recognize.

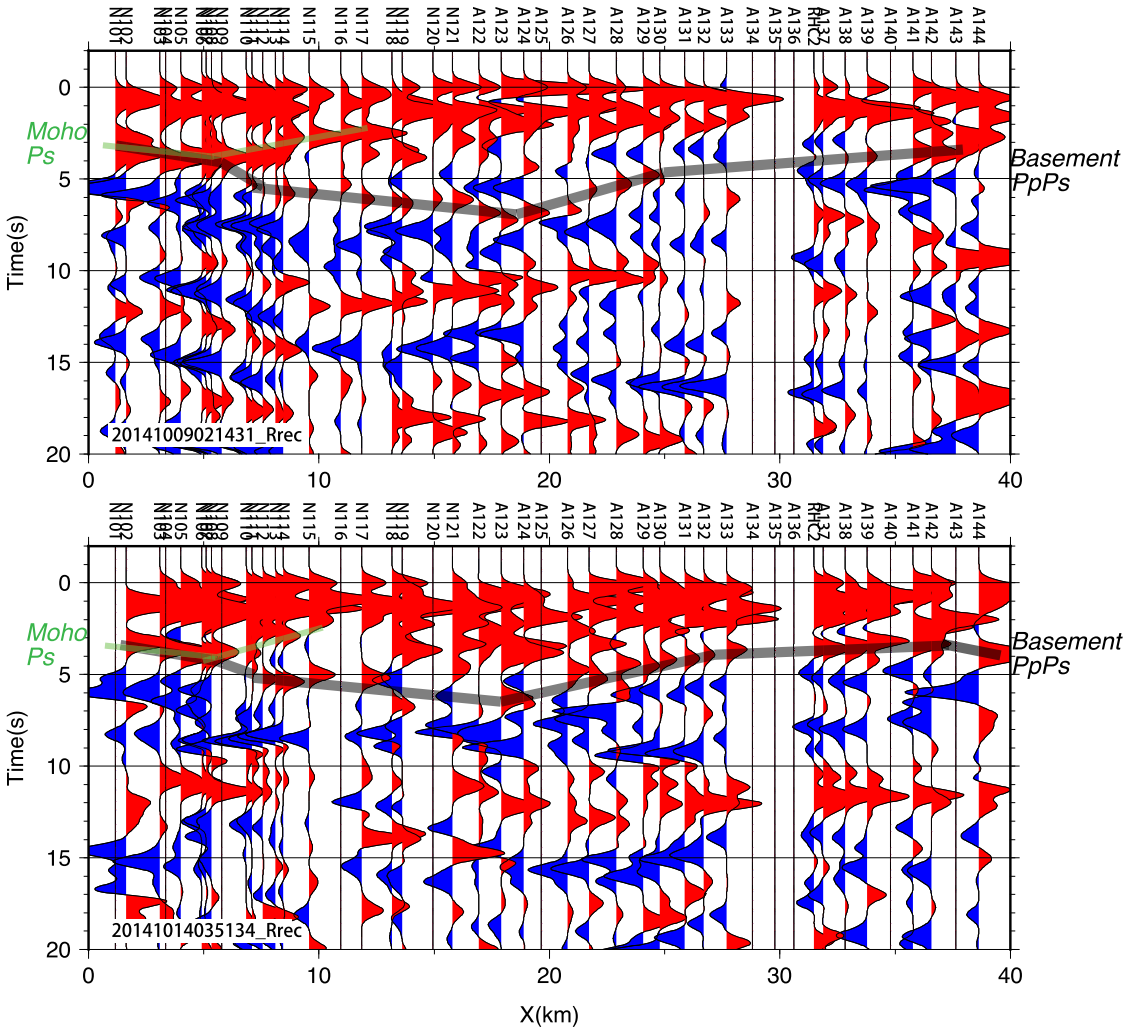

Figure 2. Receiver functions of two events recorded by all the yellow dot stations in Fig. 1. The *PpPs* phase related to the *P*-to-*S* conversion at the basement is recognized after the time–depth conversion shown in Fig. S2 in the Supporting Information. The event information is in Table 1.

3 AMBIENT NOISE TOMOGRAPHY

3.1 Phase velocity maps

Love and Rayleigh waves from tangential- and vertical-component cross-correlations, respectively, are used to invert for the shear velocities. While the Love wave in the range of 1–10 s period, is relatively simple for dispersion analysis, a strong first higher mode Rayleigh wave exists for periods less than 5 s, which complicates the use of fundamental-mode Rayleigh wave Ma *et al.* (2016). As was proposed in Ma *et al.* (2016), we use the particle motion direction, which is retrograde for fundamental and prograde for higher mode, to separate the two modes. For high frequencies (∼1 s), we may not observe the prograde higher mode as it changes sign to retrograde, in which case, we separate the two modes in the middle of the two peaks in the envelope.

The FTAN method (Bensen *et al.* 2007; Lin *et al.* 2008) is used to measure the phase velocity dispersion curves for both the Love wave and the fundamental-mode Rayleigh wave after muting the higher mode. To resolve the 2π ambiguity, we track the dispersion curve from long period to short period, and use the group velocity ($U = \partial w/\partial k$) to guide the instantaneous slope of the dispersion curve. The longest period used for each station pair is limited by one wavelength (Luo *et al.* 2015) to satisfy the far-field approximation.

The dispersion curves are used to invert for the phase velocity maps at each period, with a method similar to Barmin *et al.* (2001). The tomographic inversion is formed as a linear inversion problem to minimize the cost function of $(Gm - d)^T C^{-1}(Gm - d) + \lambda^2 Fm^2$, where the first term is the data misfit with the data covariance matrix C estimated from the misfit after a trial inversion (with a large damping parameter) and the second term is the Gaussian smoothness with the correlation length set as twice the grid size. The damping parameter λ is chosen with reference to the L-curve (misfit versus smoothness curve) (Aster *et al.* 2012). The resolution matrix $R = (G^T C^{-1} G + \lambda^2 F^T F)^{-1} G^T C^{-1} G$ is used to do the resolution test, with the input checkerboard model m and output model $\hat{m} = Rm$.

We measure the dispersion curves from 1 to 10 s for the cross-correlations between the LASSIE stations. The dispersion curves are then used to form the phase velocity maps at each period through tomographic inversion on a 2-km grid. Because of the one-wavelength criteria, the number of rays generally decreases with period, and is fewer for the Rayleigh wave because of a higher velocity especially at periods longer than 5 s when it becomes

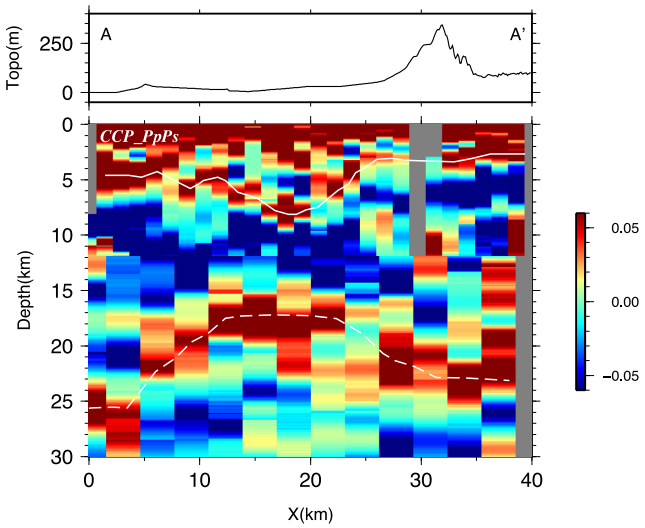

Figure 3. CCP migration with *PpPs* phase. The white lines delineate the inferred basement and Moho depths.

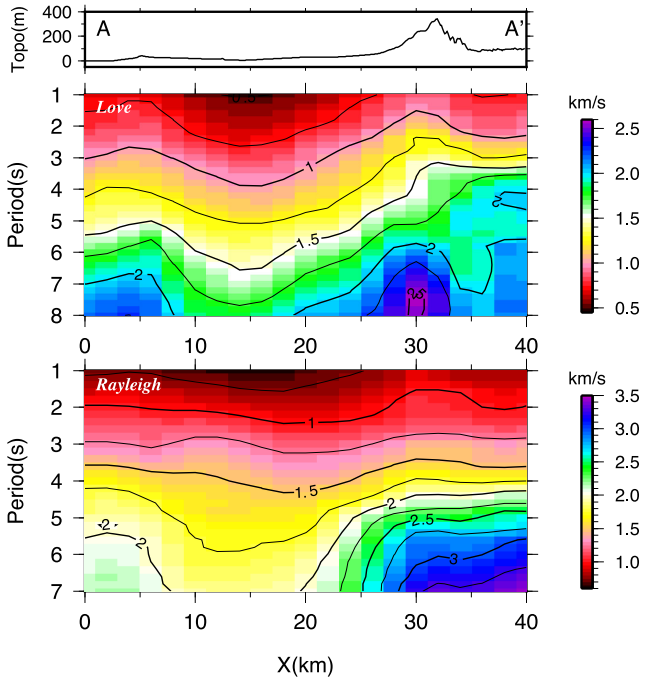

Figure 4. Tomographic inversion result along A–A′ profile. The *y*-axis is the period.

sensitive to the basement. Based on the results from the resolution test (Fig. S4, Supporting Information), we use the Love wave to 8 s and the Rayleigh wave to 7 s period. A 2-D profile (distance versus period) along A–A′ is extracted and shown in Fig. 4.

In Figs S5 and S6 in the Supporting Information, we show the phase velocity maps (5–10 s) for the entire region of Fig. 1, with a grid size of 5 km used in the inversion. While the LASSIE array enhances the resolution of Figs S5 and S6, the SCSN stations do not contribute significantly to improving the resolution along A–A′, because the density of the LASSIE survey is much higher than the SCSN network. Therefore, we only use the phase velocities shown in Fig. 4 for the shear velocity inversions.

3.2 Shear velocity structure

The dispersion curve at each location along A–A′ profile is then extracted from the phase velocity maps, and inverted for the local 1-D structures which are then combined to form a 2-D profile. The inversion from phase velocities (c) to shear velocities (β) is a non-linear problem (Aki & Richards 2002). Haney & Tsai (2015) derived a linear form for the inversion ($c^2 = G\beta^2$) with approximate eigenfunctions calculated from a power-law structure. It has advantages that no initial model is needed, and the resolution and other properties (such as parametrization of the layers and choice of damping parameters) are simpler to analyse. Other assumptions include constant density and a Poisson's ratio of 0.25 chosen to derive some of the formulae therein, which should only cause small errors in the result because the phase velocities are most sensitive to *Vs*.

Using the method of Haney & Tsai (2015), we perform a linear inversion to produce the initial model for the non-linear inversion that follows. For every 1 km in the profile in Fig. 4, we extract the Love and Rayleigh wave dispersion curves, and invert for the local 1-D V_{SH} and V_{SV} structures, respectively. The model is parametrized into layers with increasing layer-thickness $h_n = \gamma k^{n-1} h_0$ ($n = 1, \ldots, N$) down to a depth of 10 km for Love wave and 15 km for Rayleigh wave, below which, it is treated as a half-space. We choose $h_0 = 0.1$ km and $\gamma k = 1.1$, and the resolution matrix (an example is shown in Fig. S7, Supporting Information) shows that the resolution is diminishing below ∼3 km for Love and ∼6 km for Rayleigh wave. Based on the V_S from the linear inversion, we calculate the *Vp* and density with the empirical relationship from Brocher (2005) (eqs 1 and 9). These are used as an initial model in the non-linear inversion code by Herrmann & Ammon (2002), and the result is shown in Fig. 5, which is only slightly different from the linear inversion result (Fig. S8, Supporting Information).

4 DISCUSSION

4.1 The basement and Moho depths

Since industry reflection data do not penetrate to the bottom of the deepest part of the basin, previous estimates of the basin bottom were determined by gravity, constrained by a few borehole measurements (McCulloh 1960; Yerkes *et al.* 1965). Here, we have provided a direct image of the basement depth with the *PpPs* phase of the RFs. We have also determined the Moho shape, which was unknown before this study.

The Moho depth beneath the Los Angeles basin has not been well resolved. The CVM-H model (Fig. S1, Supporting Information) is a simple linear interpolation between the Moho depth at the offshore and the northern edge of the basin. There have been some indication of an upwarp of the Moho beneath the basin based on the traveltime residues of the teleseismic events (Kohler & Davis 1997), however, the accuracy is limited by limited knowledge of the crustal velocities. The RF results presented here directly show the elevated Moho shape beneath the basin, and reveal a 10 km thick crust (excluding the sediments) in the central of the basin.

We can show that the basin is in isostatic equilibrium from the following analysis. Denote the density of the sediment, crust and mantle as ρ_s, ρ_c and ρ_m; the initial thickness of the crust before stretching as h_c; the thickness of the sediments as h_s; and the elevation of the Moho beneath the basin (filled by mantle) as h_m. From the principle of isostasy, we have: $\rho_c h_c = \rho_s h_s + \rho_c (h_c - h_s - h_m) + \rho_m h_m$.

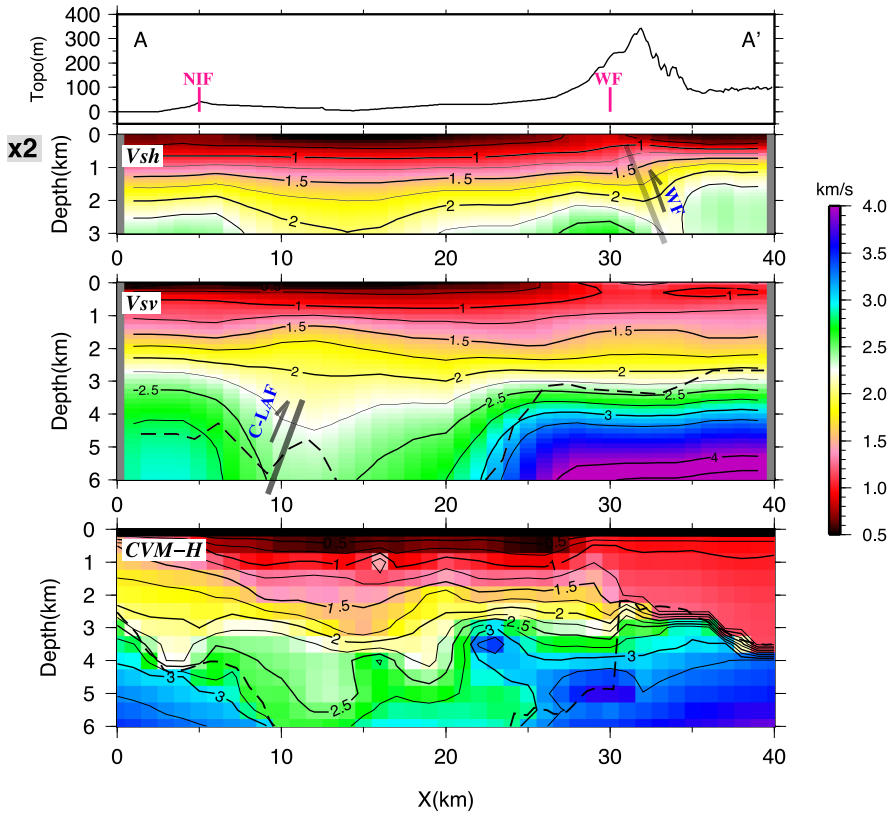

Figure 5. Inversion results using 1–8 s Love wave and 1–7 s Rayleigh wave dispersion data. The black dashed line is the basement depth from the RFs. Also shown is the CVM-H model (bottom panel).

This gives $h_s/h_m = \Delta h_s/\Delta h_m = (\rho_m - \rho_c)/(\rho_c - \rho_s)$, which is 5/3 for $\rho_s = 2500$ kg m^{-3}, $\rho_c = 2800$ kg m^{-3} and $\rho_m = 3300$ kg m^{-3}. We determine $\Delta h_s/\Delta h_m$ from the RFs, which is about 1. It is within the reasonable range of the prediction by isostasy (e.g. using $\rho_m = 3100$ kg m^{-3} or $\rho_s = 2300$ kg m^{-3}).

Using $h_s/h_m = \Delta h_s/\Delta h_m = 1$ and the observed h_s, we estimate that the initial crustal thickness is about 26 km. In the CVM-H model, since the Moho beneath the basin is an interpolation from the Moho outside of the basin, it may approximate the Moho before stretching. We see that our estimate is indeed about the average of the CVM-H model here (Fig. S1, Supporting Information). The stretch factor β, which is the ratio between the original and the thinned crustal thickness, is thus 2.6 for the centre of the basin, and decreases to about 1.3 at the edge. This factor determines the thermal subsidence of the basin in the uniform stretching model of McKenzie (1978). Using formulae and parameters in McKenzie (1978) with an assumption of a sediment-loaded basin and the starting of thermal subsidence at about 11 Ma (Turcotte & McAdoo 1979; Sawyer *et al.* 1987), we estimate that the deficiency of the prediction is ∼3 km in the centre and 1 km in the edge. Sawyer *et al.* (1987) suggested that even an infinite β is insufficient to explain the rapid thermal subsidence and the thermal conduction in a 2-D model (which is 1-D in the original model) is needed. The stretch ratio, however, is a variable that needs to be estimated in their paper, and our results can be used to better constrain the model.

4.2 The shear velocities

The ambient-noise Love and Rayleigh waves provide constraints on V_{SH} to 3 km and V_{SV} to 6 km depths, respectively, due to their different depth sensitivities. Fig. 5 shows our results along with the CVM-H model. In Fig. S9 in the Supporting Information, we in addition show a geological profile that is close to A–A′ (E–E′ in Wright 1991) for comparison, and a detailed profile around the Puente Hills can be found in Bjorklund & Burke (2002) (C–C′ therein). Note that, the *S*-wave velocity in CVM-H is largely inferred from the *P*-wave velocity from the oil industry, and therefore, shows a lot of detail that it inherits from V_P. In contrast, we provide direct measurements on the shear velocities.

The V_{SH} (Fig. 5a) and V_{SV} (Fig. 5b) results in the top 3 km are similar, except at the distance range larger than 32 km (north of the Puente Hills) where V_{SH} is considerably (∼0.5 km s^{-1}) higher than V_{SV}. The high V_{SH} can be related with the thrusting basement rocks along the Whittier fault (Bjorklund & Burke 2002). From an oil-company survey in the western Puente Hills, the Puente Hills are underlain by an aggregate of about 5 km of Cenozoic rocks which overlies a Mesozoic basement of granitoid plutonic rocks that contain a large pendant of foliated greenschist (Yerkes 1972). Although the schist generally has a strong anisotropy (Godfrey *et al.* 2000), the V_{SV} does not show the signature of the schist as a higher velocity at 2–3 km depth range, and hence we think the resolution is deficient for the Rayleigh wave here and the apparent anisotropy ($V_{SH} > V_{SV}$) is not likely true.

At a depth below 4 km, the basement beneath the Puente Hills and the San Gabriel Valley show unusually high V_{SV}velocity (∼4 km s^{-1}), which is in accordance with the schist mentioned above. The high velocity basement has been previously revealed in V_P (Lutter *et al.* 1999; Fuis *et al.* 2001; Lee *et al.* 2014), which can be higher than 7 km s^{-1} in some locations (Lutter *et al.* 1999;

Lee *et al.* 2014) and have been interpreted as rocks of the Peninsula Ranges batholith (Lutter *et al.* 1999).

We also note the depression of the velocity contour in the 3–6 km depth range at 10 km distance. This coincides with the location of the buried Compton-Los Alamitos fault in Wright (1991) ('C-LAF' in Fig. S9, Supporting Information). A small depression in the basement depth at 10 km distance can also be observed in the CCP (Fig. 3) and depth-domain RFs (Fig. S2, Supporting Information).

5 CONCLUSIONS

We used data from a dense but short duration (∼1.5 month) array that was deployed across the LA Basin to image the structure of the basin. The basement and Moho depths are clearly delineated by the *PpPs* phase in the RFs from two teleseismic events. The shear velocities are inferred from the Love and Rayleigh waves that emerge in the multicomponent cross-correlations.

An elevated Moho is imaged beneath the basin. From the edge to the centre of the basin, the basement depth increase from about 3–4 km to about 8 km and the crystalline crustal thickness decreases from 20 to 10 km. It indicates a stretch factor increasing from 1.3 to 2.6, with an estimated initial crustal thickness of 26 km from isostasy.

The deep buried Compton-Los Alamitos fault is evident from both the V_{SV} and the RF results, and the Whittier thrust fault is evident from the V_{SH} profile. An unusually high (∼4.0 km s^{-1}) shear velocity is observed in the basement beneath the Puente Hills–San Gabriel Valley, which shows the presence of the schist, and is distinct from the basement to the south.

ACKNOWLEDGEMENTS

We thank our partners in the LASSIE survey: Nodalseismic (Dan Hollis and Mitchell Barklage), USGS (Elizabeth Cochran), UCLA (Paul Davis) and CalPoly Pomona (J. Polet). This project was partially supported by the USGS/Caltech Cooperative Agreement G14AC00109 and SCEC Project 15018.

REFERENCES

Aki, K. & Richards, P.G., 2002. *Quantitative Seismology*, University Science Books.

Aster, R.C., Borchers, B. & Thurber, C.H., 2012. *Parameter Estimation and Inverse Problems,* Academic Press.

Barmin, M.P., Ritzwoller, M.H. & Levshin, A.L., 2001. A fast and reliable method for surface wave tomography, *Pure appl. Geophys.,* **158,** 1351–1375.

Bensen, G.D., Ritzwoller, M.H., Barmin, M.P., Levshin, A.L., Lin, F., Moschetti, M.P., Shapiro, N.M. & Yang, Y., 2007. Processing seismic ambient noise data to obtain reliable broad-band surface wave dispersion measurements, *Geophys. J. Int.,* **169,** 1239–1260.

Bjorklund, T. & Burke, K., 2002. Four-dimensional analysis of the inversion of a half-graben to form the Whittier fold–fault system of the Los Angeles basin, *J. Struct. Geol.,* **24,** 1369–1387.

Brocher, T.M., 2005. Empirical relations between elastic wavespeeds and density in the Earth's crust, *Bull. seism. Soc. Am.,* **95,** 2081–2092.

Crouch, J.K. & Suppe, J., 1993. Late Cenozoic tectonic evolution of the Los Angeles basin and inner California borderland: a model for core complex-like crustal extension, *Bull. geol. Soc. Am.,* **105,** 1415–1434.

Fuis, G., Ryberg, T., Godfrey, N., Okaya, D. & Murphy, J., 2001. Crustal structure and tectonics from the Los Angeles basin to the Mojave Desert, southern California, *Geology,* **29,** 15–18.

Godfrey, N.J., Christensen, N.I. & Okaya, D.A., 2000. Anisotropy of schists: contribution of crustal anisotropy to active source seismic experiments and shear wave splitting observations, *J. geophys. Res.,* **105,** 27 991–28 007.

Haney, M.M. & Tsai, V.C., 2015. Nonperturbational surface-wave inversion: a Dix-type relation for surface waves, *Geophysics,* **80,** EN167–EN177.

Hauksson, E., 2000. Crustal structure and seismicity distribution adjacent to the Pacific and North America plate boundary in southern California, *J. geophys. Res.,* **105,** 13 875–13 903.

Herrmann, R. & Ammon, C., 2002. *Computer Programs in Seismology: Surface Waves, Receiver Functions and Crustal Structure,* St. Louis University.

Ingersoll, R.V. & Rumelhart, P.E., 1999. Three-stage evolution of the Los Angeles basin, southern California, *Geology,* **27,** 593–596.

Jennings, C.W. & Bryant, W.A., 2010. Fault activity map of California: California Geological Survey, Geologic Data Map Series No. 6, map scale 1:750 000.

Kohler, M.D. & Davis, P.M., 1997. Crustal thickness variations in southern California from Los Angeles Region Seismic Experiment passive phase teleseismic travel times, *Bull. seism. Soc. Am.,* **87,** 1330–1344.

Komatitsch, D., Liu, Q., Tromp, J., Süss, P., Stidham, C. & Shaw, J.H., 2004. Simulations of ground motion in the Los Angeles basin based upon the spectral-element method, *Bull. seism. Soc. Am.,* **94,** 187–206.

Lee, E.J., Chen, P., Jordan, T.H., Maechling, P.B., Denolle, M.A. & Beroza, G.C., 2014. Full-3-D tomography for crustal structure in Southern California based on the scattering-integral and the adjoint-wavefield methods, *J. geophys. Res.,* **119,** 6421–6451.

Ligorría, J.P. & Ammon, C.J., 1999. Iterative deconvolution and receiver-function estimation, *Bull. seism. Soc. Am.,* **89,** 1395–1400.

Lin, F.-C., Moschetti, M.P. & Ritzwoller, M.H., 2008. Surface wave tomography of the western United States from ambient seismic noise: Rayleigh and Love wave phase velocity maps, *Geophys. J. Int.,* **173,** 281–298.

Luo, Y., Yang, Y., Xu, Y., Xu, H., Zhao, K. & Wang, K., 2015. On the limitations of interstation distances in ambient noise tomography, *Geophys. J. Int.,* **201,** 652–661.

Lutter, W.J., Fuis, G.S., Thurber, C.H. & Murphy, J., 1999. Tomographic images of the upper crust from the Los Angeles basin to the Mojave Desert, California: results from the Los Angeles Region Seismic Experiment, *J. geophys. Res.,* **104,** 25 543–25 565.

Ma, Y. & Clayton, R.W., 2015. Flat slab deformation caused by interplate suction force, *Geophys. Res. Lett.* **42,** 7064–7072.

Ma, Y., Clayton, R.W. & Li, D., 2016. Higher-mode ambient-noise Rayleigh waves in sedimentary basins, *Geophys. J. Int.,* doi:10.1093/gji/ggw235.

Magistrale, H., Day, S., Clayton, R.W. & Graves, R., 2000. The SCEC Southern California reference three-dimensional seismic velocity model version 2, *Bull. seism. Soc. Am.,* **90,** S65–S76.

McCulloh, T.H., 1960. *Gravity Variations and the Geology of the Los Angeles Basin of California,* U.S. Geol. Surv. Prof. Paper 400-B, pp. 320–325.

McKenzie, D., 1978. Some remarks on the development of sedimentary basins, *Earth planet. Sci. Lett.,* **40,** 25–32.

Nicholson, C., Sorlien, C.C., Atwater, T., Crowell, J.C. & Luyendyk, B.P., 1994. Microplate capture, rotation of the western Transverse Ranges, and initiation of the San Andreas transform as a low-angle fault system, *Geology,* **22,** 491–495.

Olsen, K., 2000. Site amplification in the Los Angeles basin from three-dimensional modeling of ground motion, *Bull. seism. Soc. Am.,* **90,** S77–S94.

Sawyer, D.S., Hsui, A.T. & Toksöz, M.N., 1987. Extension, subsidence and thermal evolution of the Los Angeles Basin—a two-dimensional model, *Tectonophysics,* **133,** 15–32.

Shaw, J.H. *et al.*, 2015. Unified structural representation of the southern California crust and upper mantle, *Earth planet. Sci. Lett.,* **415,** 1–15.

Süss, M.P. & Shaw, J.H., 2003. P wave seismic velocity structure derived from sonic logs and industry reflection data in the Los Angeles basin, California, *J. geophys. Res.,* **108**(B3), 2170, doi:10.1029/2001JB001628.

Tape, C., Liu, Q., Maggi, A. & Tromp, J., 2009. Adjoint tomography of the southern California crust, *Science,* **325,** 988–992.

Turcotte, D. & McAdoo, D., 1979. Thermal subsidence and petroleum generation in the southwestern block of the Los Angeles Basin, California, *J. geophys. Res.,* **84,** 3460–3464.

Wright, T.L., 1991. Structural geology and tectonic evolution of the Los Angeles Basin, California, *Act. Margin Basins,* **52,** 35–134.

Yerkes, R.F., 1972. *Geology and Oil Resources of the Western Puente Hills Area, Southern California*, U.S. Geol. Surv. Prof. Paper 420-C, pp. 1–63.

Yerkes, R.F., McCulloh, T.H., Schoellhamer, J. & Vedder, J.G., 1965. *Geology of the Los Angeles Basin, California: An Introduction*, U.S. Geol. Surv. Prof. Paper 420-A, pp. 1–57.

Zhu, L., 2000. Crustal structure across the San Andreas Fault, southern California from teleseismic converted waves, *Earth planet. Sci. Lett.,* **179,** 183–190.

Zhu, L. & Kanamori, H., 2000. Moho depth variation in southern California from teleseismic receiver functions, *J. geophys. Res.,* **105,** 2969–2980.

SUPPORTING INFORMATION

Additional Supporting Information may be found in the online version of this paper:

Figure S1. CVM-H model along profile A–A′. The white lines delineate the basement and Moho depths.

Figure S2. The depth-axis RFs with time–depth conversion for *PpPs* phase. The ∼5 km offset in the structures on the two profiles are due to the different piercing points of the two events (Fig. 1), which is corrected in the CCP profile (Fig. 3).

Figure S3. The time-axis RFs for DLA station. The events are arranged according to the backazimuths, and are divided by four quadrants (red-pink dots). The coloured bar along the *x*-axis divides the quadrants.

Figure S4. Love and Rayleigh wave tomography resolution test, using LASSIE stations only. Similar as the tomography results in Fig. 4, the resolution test is performed at each period, and the results along A–A′ profile are extracted and combined to show here.

Figure S5. Love wave phase velocity maps and resolutions test from 5 to 10 s, using both LASSIE and SCSN stations.

Figure S6. Rayleigh wave phase velocity maps and resolutions test from 5 to 10 s, using both LASSIE and SCSN stations.

Figure S7. The resolution matrix (estimated from the linear inversion in Fig. S8) for the 1-D inversion at $x \approx 0$ km. The Love wave inversion has a good resolution until 3 km depth, and the Rayleigh wave inversion has a good resolution until 6 km depth.

Figure S8. (a) The linear inversion results using method by Haney & Tsai (2015). See the text for more detail. (b) The rms error compared with the non-linear inversion result in Fig. 5. The non-linear inversion results better fit the dispersion curves.

Figure S9. A geological profile adapted from Wright (1991). The red line shows the approximate range of A–A′.

(http://gji.oxfordjournals.org/lookup/suppl/doi:10.1093/gji/ggw236/-/DC1).

Please note: Oxford University Press is not responsible for the content or functionality of any supporting materials supplied by the authors. Any queries (other than missing material) should be directed to the corresponding author for the paper.